Time-reversal invariant realization of the Weyl semimetal phase

Gábor B. Halász[1,2] and Leon Balents[1]

[1]*Kavli Institute for Theoretical Physics, University of California, Santa Barbara, California 93106, USA*
[2]*Trinity College, University of Cambridge, Trinity Street, Cambridge CB2 1TQ, United Kingdom*

We propose a realization of the Weyl semimetal phase that is invariant under time reversal and occurs due to broken inversion symmetry. We consider both a simple superlattice model and a more realistic tight-binding model describing an experimentally reasonable HgTe/CdTe multilayer structure. The two models have the same underlying symmetry, therefore their low-energy features are equivalent. We find a Weyl semimetal phase between the normal insulator and the topological insulator phases that exists for a finite range of the system parameters and exhibits a finite number of Weyl points with robust band touching at the Fermi level. This phase is experimentally characterized by a strong conductivity anisotropy and topological surface states. The principal conductivities change in a complementary fashion as the system parameters are varied, and the surface states only exist in a region of momentum space that is determined by the positions of the Weyl points.

PACS number(s): 03.65.Vf, 73.21.Cd, 73.20.−r

I. INTRODUCTION

In recent decades, topological phases of matter have been in the focus of intense theoretical and experimental study; for a review, see Ref. 1 and references therein. The order exhibited by these phases is not associated with spontaneous symmetry breaking, and it can be described by topological invariants that are insensitive to smooth changes in the system parameters.[2] As a generic feature, these phases also have topologically protected edge states.

The field of topological phases was revolutionized by the discovery of two-dimensional (2D) topological insulators,[3,4] and the subsequent generalization to three-dimensional (3D) topological insulators.[5] These materials exhibit a bulk energy gap between the valence and the conduction bands, similarly to normal insulators. On the other hand, they have gapless surface states that are topologically protected, therefore conduction is possible on the surface. Since topological insulators arise due to strong spin-orbit coupling, their prevalence is larger within materials consisting of heavier elements.[6] They find potential applications in the areas of spintronics and quantum computation.

It is a recent development that topologically protected surface states can also be achieved in materials without a bulk energy gap: these are the Weyl semimetals.[7–9] They have band touching between the conduction and the valence bands at the Fermi level. The band-touching points are called Weyl points because the dispersion relation around them is linear and hence the excitations are equivalent to Weyl fermions. Weyl points can have positive or negative helicities, and they always appear in pairs. To achieve robust band touching that cannot be removed by an infinitesimal perturbation, Weyl points of opposite helicities must be separated in momentum space.[8] This requires breaking either the time-reversal or the inversion symmetry of the system.[10]

Recent papers on Weyl semimetals have predominantly studied the case with broken time-reversal symmetry.[7,8] One notable exception is Ref. 9, where time-reversal symmetry remains intact and inversion symmetry is broken. It was argued that a gapless phase appears in three dimensions between the normal insulator (NI) and the topological insulator (TI)

phases. In this paper, we are also interested in the time-reversal invariant case, but address specifically how this phase, which is in fact the Weyl semimetal, may be designed in a NI/TI superlattice. We propose two models: a simple superlattice model adapted from Ref. 8 and a more realistic tight-binding model describing a HgTe/CdTe multilayer structure. The former model is presented in Sec. II and the latter one is presented in Sec. III. The most prominent experimental features are discussed in Sec. IV, while the overall conclusions of the paper are summarized in Sec. V.

II. SUPERLATTICE MODEL

A. General description

The model considered in this section is based on the multilayer structure in Ref. 8: a periodic superlattice of NI and TI layers grown in the z direction. It is a simplified tight-binding model where we only take the surface states located at the NI/TI interfaces into account. These states are labeled by the unit cell index and the parallel 2D momentum $\mathbf{k} = (k_x, k_y)$.

It is known that a realization of the Weyl semimetal phase requires breaking either the time-reversal or the inversion symmetry of the system. Since we intend to keep the time-reversal symmetry intact, the inversion symmetry must be broken. To achieve that, we introduce a finite voltage V between the top and the bottom NI/TI interfaces in each unit cell. The Hamiltonian of the multilayer structure is then

$$H = \sum_{\mathbf{k}} \sum_{i,j} \left[v_F \tau^z (\sigma^x k_y - \sigma^y k_x) \delta_{i,j} + V \tau^z \delta_{i,j} \right.$$
$$\left. + \Delta_T \, \tau^x \delta_{i,j} + \Delta_N \sum_{\pm} \tau^{\pm} \delta_{i,j\pm 1} \right] c_{i,\mathbf{k}}^{\dagger} c_{j,\mathbf{k}}, \quad (1)$$

where the Pauli matrices $\vec{\sigma} = (\sigma^x, \sigma^y, \sigma^z)$ act on the real spin degree of freedom and the Pauli matrices $\vec{\tau} = (\tau^x, \tau^y, \tau^z)$ act on the top/bottom surface pseudospin degree of freedom. The first term describes the NI/TI surface states with isotropic Fermi velocity v_F, the second term represents the inversion-breaking

voltage, and the remaining terms describe hopping between neighboring interfaces. The hopping amplitude through a TI layer is Δ_T and that through a NI layer is Δ_N. In general, both Δ_T and Δ_N can be functions of the parallel momentum $\mathbf{k}$, and the symmetries of these functions determine the symmetry of the system.

The Hamiltonian in Eq. (1) can be solved by exploiting the translational symmetry in the z direction, and introducing the corresponding 3D momentum $\vec{k} = (k_x, k_y, k_z)$. By doing so, we find that the band dispersion relation is

$$E_\pm^2(\vec{k}) = \Delta^2(k_z) + [V \pm v_F|\mathbf{k}|]^2, \quad (2)$$

where $\Delta(k_z) = \sqrt{\Delta_T^2 + \Delta_N^2 + 2\Delta_T\Delta_N\cos(k_zd)}$ and d is the periodicity of the superlattice. The four bands are nondegenerate when $\mathbf{k} \neq 0$, and band touching between the two middle bands takes place when $E_- = 0$. If we assume without loss of generality that Δ_T and Δ_N are both positive, this happens when $k_zd = \pi$, $\Delta_T = \Delta_N$, and $V = v_F|\mathbf{k}|$.

B. The Weyl semimetal phase

If Δ_T and Δ_N are independent of $\mathbf{k}$, the band touching occurs along a circle of radius V/v_F in the $k_z = \pi/d$ plane. It marks the transition between the NI and the TI phases of the material at $\Delta_T = \Delta_N$. We can argue on physical grounds that $\Delta_T > \Delta_N$ (thin TI layers and thick NI layers) corresponds to the NI phase, while $\Delta_T < \Delta_N$ (thick TI layers and thin NI layers) corresponds to the TI phase.

However, this band touching is not robust because it requires the fine tuning of the condition $\Delta_T = \Delta_N$. To achieve robust band touching, we need to make the hopping amplitudes depend on the momentum $\mathbf{k}$:

$$\Delta_{T,N} = \Delta_{T,N}^{(0)} + \Delta_{T,N}^{(1)}(\mathbf{k}). \quad (3)$$

Furthermore, we cannot keep the continuous rotational symmetry around the z axis because then Δ_T and Δ_N are still constants at $|\mathbf{k}| = V/v_F$, the only region where band touching is possible. On the other hand, the continuous rotational symmetry is broken in real crystals as well, and one is only left with a discrete rotational symmetry. In the following, we demonstrate robust band touching in the reasonable cases of the fourfold and twofold rotational symmetries.

C. Fourfold rotational symmetry

In the first case, we assume a fourfold rotational symmetry around the z axis and four planes of reflection symmetry: the $\{x,z\}$ plane, the $\{y,z\}$ plane, and the two planes halfway in between. These are the natural symmetries of many real materials with tetragonal crystal structures. By neglecting any contributions depending on $|\mathbf{k}|$ only, the lowest-order term having all the above symmetries and time-reversal symmetry is $\propto(k_x^4 + k_y^4)$. The $\mathbf{k}$-dependent parts of the hopping amplitudes are then

$$\Delta_{T,N}^{(1)}(\mathbf{k}) = \delta_{T,N}|\mathbf{k}|^4(\cos^4\theta + \sin^4\theta), \quad (4)$$

where the polar coordinates $k_x = |\mathbf{k}|\cos\theta$ and $k_y = |\mathbf{k}|\sin\theta$ are introduced. The difference $\Delta_T - \Delta_N$ depends on the angle θ at $|\mathbf{k}| = V/v_F$, therefore band touching with $\Delta_T = \Delta_N$ only occurs at specific points of the circle. The band touching also

becomes robust because the parameters $\Delta_{T,N}^{(0)}$ and $\delta_{T,N}$ do not require fine tuning: an infinitesimal change in any of them only gives an infinitesimal change in θ, displacing the band-touching points along the circle.

Contrary to the case with continuous rotational symmetry, now there is a Weyl semimetal phase between the NI and the TI phases that exists for a finite range of the parameter values. This phase features a finite number of Weyl points at which band touching between the two middle bands occurs. To be more precise, the solution of the band-touching equation $\Delta_T = \Delta_N$ for the angle θ is

$$\cos(4\theta) = \frac{4(\Delta_N^{(0)} - \Delta_T^{(0)})}{|\mathbf{k}|^4(\delta_T - \delta_N)} - 3. \quad (5)$$

This expression gives eight Weyl points, which are related to each other by the symmetry transformations of the system. Since $|\cos(4\theta)| \leqslant 1$, the condition for the Weyl semimetal phase becomes $1/2 < (\Delta_N^{(0)} - \Delta_T^{(0)})/[|\mathbf{k}|^4(\delta_T - \delta_N)] < 1$, where $|\mathbf{k}| = V/v_F$ as always in this subsection. Let us assume without loss of generality that $\delta_T > \delta_N$, and imagine decreasing $\Delta_T^{(0)}$ gradually while keeping the other parameters constant. This corresponds to a transition from the NI phase to the TI phase. The Weyl points then first appear at the lines $k_x = \pm k_y$, move along the circle of radius V/v_F, and finally disappear at the lines $k_x = 0$ and $k_y = 0$. For an illustration of this, see the top half of Fig. 1.

It can be verified that the band-touching points occurring in this scenario are indeed proper Weyl points around which the band dispersion is linear in all directions. To obtain physically
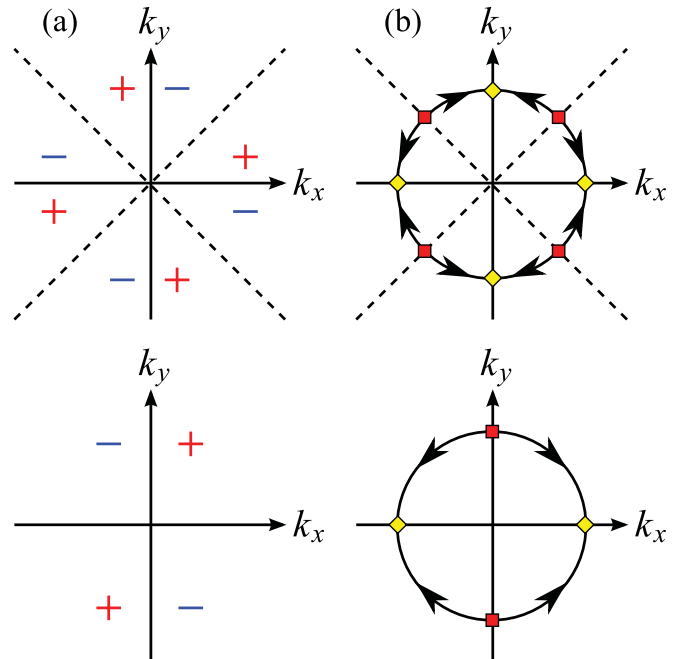

FIG. 1. (Color online) Illustration of the Weyl semimetal phase in the cases of fourfold (top) and twofold (bottom) rotational symmetries. We set $k_z = \pi/d$ in all subfigures. (a) Arrangement of the Weyl points with positive (red plus) and negative (blue minus) helicities. (b) Trajectories of the Weyl points as the transition from the NI phase to the TI phase takes place. The Weyl points first appear at the red squares and finally disappear at the yellow diamonds.

transparent results, we assume that $\delta_T - \delta_N$ is sufficiently small so that $\Delta_T - \Delta_N$ is almost independent of θ. This difference is then only important along circles of constant k_z and $|\mathbf{k}|$ where there would be no difference otherwise. Consequently, the principal directions are the axial (z), the radial (r), and the tangential (t) directions, and an expansion of E_- around a band-touching point reads

$$E_-^2(\vec{k}) = v_z^2 \delta k_z^2 + v_r^2 \delta k_r^2 + v_t^2 \delta k_t^2, \tag{6}$$

where the effective Fermi velocities corresponding to the principal directions are $v_z = d\sqrt{\Delta_T \Delta_N} = d\Delta_T$, $v_r = v_F$, and $v_t = |\mathbf{k}|^3 (\delta_T - \delta_N)|\sin(4\theta)|$. The expression in Eq. (6) indeed gives a linear band dispersion in all directions. We can now establish that the approximation of small $\delta_T - \delta_N$ requires $v_t \ll v_r$, i.e., $V^3(\delta_T - \delta_N) \ll v_F^4$. This is satisfied in the reasonable case when the inversion-breaking voltage V and the coefficients $\delta_{T,N}$ are small.

We note that the Weyl points related to each other by rotations have identical helicities, while those related to each other by reflections have opposite helicities: this implies that there are four Weyl points of each helicity. If we pair up all the Weyl points into pairs of opposite helicities, the sum of the resulting separation vectors is zero. This property follows from the general notion of time-reversal symmetry, which also implies that the anomalous Hall conductivity vanishes.

D. Twofold rotational symmetry

In the second case, we have a twofold rotational symmetry around the z axis and two planes of reflection symmetry: the $\{x,z\}$ plane and the $\{y,z\}$ plane. This case is particularly important for us because the tight-binding model described in Sec. III has the same symmetries. The lowest-order terms obeying all these symmetries and time-reversal symmetry are $\propto (k_x^2 + k_y^2)$ and $\propto (k_x^2 - k_y^2)$. However, the former one only depends on $|\mathbf{k}|$, and hence it would not break the continuous rotational symmetry on its own. For the sake of simplicity, we consider the special case of

$$\Delta_{T,N}^{(1)}(\mathbf{k}) = \delta_{T,N} \, k_x^2 = \delta_{T,N} |\mathbf{k}|^2 \cos^2\theta, \tag{7}$$

and obtain that the solution of $\Delta_T = \Delta_N$ is

$$\cos(2\theta) = \frac{2\left(\Delta_N^{(0)} - \Delta_T^{(0)}\right)}{|\mathbf{k}|^2(\delta_T - \delta_N)} - 1. \tag{8}$$

Now there are four Weyl points in the Weyl semimetal phase that occurs when $0 < (\Delta_N^{(0)} - \Delta_T^{(0)})/[|\mathbf{k}|^2(\delta_T - \delta_N)] < 1$. If there is a transition from the NI phase to the TI phase due to a gradual decrease in $\Delta_T^{(0)}$, the Weyl points first appear at the $k_x = 0$ line, move along the circle of radius V/v_F, and finally disappear at the $k_y = 0$ line. For an illustration of this, see the bottom half of Fig. 1.

If $\delta_T - \delta_N$ is sufficiently small, the principal directions around the Weyl points are the axial, the radial, and the tangential directions. Equation (6) is therefore valid in this case as well, and the effective Fermi velocities in the principal directions are given by $v_z = d\sqrt{\Delta_T \Delta_N} = d\Delta_T$, $v_r = v_F$, and $v_t = |\mathbf{k}|(\delta_T - \delta_N)|\sin(2\theta)|$. The approximation of small $\delta_T - \delta_N$ holds when $v_t \ll v_r$, i.e., when $V(\delta_T - \delta_N) \ll v_F^2$.

III. REALISTIC TIGHT-BINDING MODEL

A. Formulation of the model

In this section, we consider a periodic multilayer structure of strained HgTe and CdTe layers which are grown on top of each other in the z direction. This model is in fact a concrete realization of the superlattice structure described in Sec. II because CdTe is a NI and HgTe becomes a TI under strain.[11] The band structures of these materials are well known, and can be reproduced with high accuracy from realistic tight-binding models. Here we adapt the ten-band tight-binding model described in Ref. 12, which assumes two s orbitals (s, s^*) and three p orbitals (p_x, p_y, p_z) on each atom.

Both HgTe and CdTe have zinc-blende structures: the anions (Te) form a face-centered-cubic lattice, and the cations (Hg, Cd) are located at the positions $\frac{1}{4}[1,1,1]$. This implies that each anion (cation) is tetrahedrally coordinated by four nearest-neighbor cations (anions). We assume that the thicknesses of the HgTe and CdTe layers are N_1 and N_2 as measured in units of the cubic lattice parameter a. When cutting through the structure along the z direction, one finds subsequent layers of one atomic thickness consisting of only anions and only cations, respectively. The anionic layers all contain Te, while there are $2N_1$ cationic layers containing Hg and $2N_2$ cationic layers containing Cd in each superlattice period.

The atomic orbitals are labeled according to $|\vec{R}, u, t, \sigma\rangle$, where $\vec{R}$ is the position of the atomic site, $u = \{Te, Hg, Cd\}$ is the type of the atom, $t = \{s, s^*, p_x, p_y, p_z\}$ is the type of the orbital, and $\sigma = \{\uparrow, \downarrow\}$ is the spin quantum number. The Hamiltonian of the system can be written as

$$H = H_0 + H_I + H_{so}, \tag{9}$$

where the first term contains the bare energies of the atomic orbitals, the second term describes the interaction (hopping) between them, and the third term represents spin-orbit coupling. These terms are

$$H_0 = \sum_{\vec{R}, t, \sigma} |\vec{R}, u(\vec{R}), t, \sigma\rangle E_{u(\vec{R}), t} \langle \vec{R}, u(\vec{R}), t, \sigma|,$$

$$H_I = \sum_{\vec{R}, t, \sigma} \sum_{\vec{R}', t'} |\vec{R}, u(\vec{R}), t, \sigma\rangle V_{u(\vec{R}), u(\vec{R}'), t, t'} \langle \vec{R}', u(\vec{R}'), t', \sigma|, \tag{10}$$

$$H_{so} = \sum_{\vec{R}, t, t' \sigma, \sigma'} |\vec{R}, u(\vec{R}), t, \sigma\rangle 2\lambda_{u(\vec{R})} \vec{L} \cdot \vec{\sigma} \langle \vec{R}, u(\vec{R}), t', \sigma'|,$$

where the second sum in H_I goes over all four nearest neighbors $\vec{R}'$ of the atomic site $\vec{R}$, and $u(\vec{R})$ denotes the type of the atom at the position $\vec{R}$.

The hopping amplitudes $V_{u,u',t,t'}$ between different types of p orbitals are related to each other by the geometry of the crystal structure. In particular, they are affected by the uniaxial strain ϵ which is defined as the relative elongation of the lattice constant in the z direction with respect to those in the x and y directions. This strain occurs because the subsequent layers of HgTe and CdTe are grown on top of each other, and there is a slight lattice-constant mismatch.[13] Since the lattice constant of CdTe is approximately 0.3% larger than that of HgTe, and both materials have a Poisson's ratio ≈ 0.5, we assume that the relationship between the strains in

TABLE I. Bare energies $E_{u,t}$ and spin-orbit coupling strengths λ_u for different atom types (all numbers are in eV units).

u	Te	Hg	Cd
$E_{u,s}$	−9.75	−1.40	−1.42
$E_{u,p}$	0.12	4.30	3.48
$E_{u,s*}$	6.08	6.50	6.67
λ_u	0.333	0.286	0.013

them is $\epsilon(\mathrm{CdTe}) = \epsilon(\mathrm{HgTe}) + 0.009$. Even if a small strain does not change the distance between neighboring atoms, the direction vector connecting them changes, leading to a different overlap between any two orbitals if at least one of them is a p orbital. Using simple geometry, the different hopping amplitudes involving p orbitals are then expressed as

$$
\begin{aligned}
V_{s,p_x} &= V_{s,p_y} = \frac{1}{\sqrt{3}} V_{s,p,\sigma} \left(1 - \frac{\epsilon}{3}\right), \\
V_{s,p_z} &= \frac{1}{\sqrt{3}} V_{s,p,\sigma} \left(1 + \frac{2\epsilon}{3}\right), \\
V_{p_x,p_x} &= V_{p_y,p_y} = \frac{1}{3}\left[V_{p,p,\sigma}\left(1 - \frac{2\epsilon}{3}\right) + 2V_{p,p,\pi}\left(1 + \frac{\epsilon}{3}\right)\right], \\
V_{p_z,p_z} &= \frac{1}{3}\left[V_{p,p,\sigma}\left(1 + \frac{4\epsilon}{3}\right) + 2V_{p,p,\pi}\left(1 - \frac{2\epsilon}{3}\right)\right], \\
V_{p_x,p_y} &= \frac{1}{3}(V_{p,p,\sigma} - V_{p,p,\pi})\left(1 - \frac{2\epsilon}{3}\right), \\
V_{p_x,p_z} &= V_{p_y,p_z} = \frac{1}{3}(V_{p,p,\sigma} - V_{p,p,\pi})\left(1 + \frac{\epsilon}{3}\right).
\end{aligned}
\tag{11}
$$

Note that the subscripts u and u' are suppressed for the sake of compactness, the label s can stand for both s and s^*, and all terms are expanded up to first order in ϵ.

The concrete tight-binding parameters are based on those in Ref. 12, but they are normalized according to a consistent procedure. The bare energies of all orbitals in the CdTe model are first shifted such that the Te orbitals have the same average energy in HgTe and CdTe. This corresponds to matching the arbitrary zero energy levels of the independent HgTe and CdTe tight-binding models. The bare energies of the respective Te orbitals are then obtained by averaging those in the normalized HgTe and CdTe models, which are already close to each other at this point. The spin-orbit coupling

TABLE II. Hopping amplitudes between different atom and orbital types (all numbers are in eV units).

u/u'	Te/Hg	Te/Cd
$V_{u,u',s,s}$	−0.817	−1.195
$V_{u,u',s,p,\sigma}$	1.044	0.753
$V_{u,u',p,s,\sigma}$	−1.404	−2.064
$V_{u,u',s*,p,\sigma}$	1.524	0.844
$V_{u,u',p,s*,\sigma}$	−0.140	−1.147
$V_{u,u',p,p,\sigma}$	2.180	2.651
$V_{u,u',p,p,\pi}$	−0.549	−0.442

strength λ_{Te} is averaged in the same way, and the final values of the tight-binding parameters are presented in Tables I and II.

Table I shows that the normalized bare energies of the Hg orbitals are on average larger than those of their Cd counterparts. The HgTe layers are therefore more positively charged than the CdTe layers, resulting in a potential difference that lowers the orbital energies in the HgTe layers. This effect is taken into account by introducing a periodic potential $U(\vec{r})$, which is added to all bare energies at position $\vec{r}$. The potential depends on z only, and we write it in the form

$$
U(z) = -U_0 \cos\left[\frac{2\pi}{d}\left(z - \frac{d_1}{2} + \delta_0\right)\right],
\tag{12}
$$

where $d_{1,2} = aN_{1,2}$ are the thicknesses of the HgTe and CdTe layers, and $d = d_1 + d_2$ is the periodicity of the superlattice. In the symmetric case when $\delta_0 = 0$, the potential function $U(z)$ reaches its minimum in the middle of the HgTe layer and its maximum in the middle of the CdTe layer. However, we assume a certain asymmetry in $U(z)$, which is characterized by the displacement δ_0 of these extrema. When the multilayer is grown under reasonable experimental conditions, such an asymmetry is inadvertently present due to the specific growth direction. For example, it is possible that the HgTe and CdTe materials are more likely to form an alloy at one of their interfaces. Since the resulting asymmetry is probably small, we take $0 < |\delta_0| < a$ in the rest of this section. Also, by comparing the bare energies in Table I we estimate that the amplitude of the potential is $U_0 \sim 0.1$ eV.

B. Linear fourband approximation

The Hamiltonian presented in Eqs. (9) and (10) can be solved by exploiting translational invariance and introducing the corresponding momentum $\vec{k} = (k_x, k_y, k_z)$. On the other hand, the large periodicity in the z direction means that the Hamiltonian is represented by a large $M \times M$ matrix where $M = 40(N_1 + N_2)$. It can therefore only be solved numerically, and for relatively small layer thicknesses $N_{1,2}$.

However, despite the complexity in this model, some of its properties can be deduced by referring to symmetry only. In the case of $U_0 \neq 0$ and $\delta_0 \neq 0$, the basic symmetries of the system are time-reversal symmetry (T) and the reflection symmetries ($\mathrm{R}_{1,2}$) across the $\{y',z\}$ and the $\{x',z\}$ planes. The natural coordinates $x' = (x + y)/\sqrt{2}$ and $y' = (x - y)/\sqrt{2}$ are introduced to make these symmetries more explicit. Note that the reflection symmetries $\mathrm{R}_{1,2}$ also lead to a twofold rotational symmetry (S) around the z axis. In terms of symmetry, the tight-binding model studied in this section is equivalent to the superlattice model in Sec. II D.

The presence of both T and S symmetries puts two crucial restrictions on the band structure. First, the states on the $k_{x'} = k_{y'} = 0$ line are twofold degenerate. Since the number of occupied bands is always even, the highest occupied band (HOB) and the lowest unoccupied band (LUB) have different energies on this line with the Fermi level lying between them. Second, the band structure is invariant under the reflection $k_z \leftrightarrow -k_z$. As shown in Sec. III C, this implies that robust band touching between the HOB and the LUB is only possible in the $k_z = 0$ and the $k_z = \pi/d$ planes.

Numerical investigation of the model indicates that band touching between the HOB and the LUB always occurs close to the $k_{x'} = k_{y'} = 0$ line. In perspective of this and of the symmetry considerations above, we introduce simplified fourband models around the two special points at $\vec{k} = (0,0,0)$ and $\vec{k} = (0,0,\pi/d)$. We only keep the nearest two bands on each side of the Fermi level, and assume that they are linear in the relative momentum $\delta\vec{k} = (k_{x'}, k_{y'}, \delta k_z)$ with respect to the corresponding special point. More formally, we project the Hamiltonian H onto a subspace spanned by four basis states: the appropriate eigenvectors of the full model at $\delta\vec{k} = 0$. The reduced Hamiltonian $\mathcal{H}$ is then a 4×4 diagonal matrix at $\delta\vec{k} = 0$, and the linearity of the band dispersion is achieved by additional terms that are linear in $\delta\vec{k}$.

At the special point, the reduced Hamiltonian can be written as $\mathcal{H}_0 = E^{(1)}\tau^{(1)} + E^{(2)}\tau^{(2)}$, where $\tau^{(1,2)} = (1 \pm \tau^z)/2$ and $E^{(1,2)}$ are the energies of the LUB and the HOB at $\delta\vec{k} = 0$. The energy levels are pairwise degenerate, and this degeneracy is split by a finite $k_{x'}$ or $k_{y'}$ but not by a finite δk_z. To represent this splitting, we need to add coupling terms between states corresponding to the same energy at $\delta\vec{k} = 0$. In the most general case, the additional terms in the Hamiltonian read

$$\mathcal{H}_S = \sum_{l=1}^{2} \tau^{(l)}\big[\alpha_x^{(l)}k_{x'}\sigma^x + \alpha_y^{(l)}k_{y'}\sigma^y\big], \qquad (13)$$

where the coefficients $\alpha_{x,y}^{(1,2)}$ can be obtained from a comparison with the full model. The choice of the Pauli matrices $\sigma^{x,y}$ corresponds to defining the basis states within the degenerate subspaces of $\mathcal{H}_0$ in a particular way.

There is also coupling between states corresponding to different energies at $\delta\vec{k} = 0$. Since the Hamiltonian $\mathcal{H}$ must be invariant under all symmetry operations of the system, there are only a small number of such coupling terms allowed by symmetry. The parities of the possible terms under the symmetry operations are summarized in Table III. Note that the parities of τ^z and $\sigma^{x,y}$ are determined by the already established terms $\mathcal{H}_0$ and $\mathcal{H}_S$, which must be even under all symmetry operations. Furthermore, the relations between different Pauli matrices imply that we only need to choose the parities of τ^x under T and $R_{1,2}$. The choice of these parities corresponds to setting the relative complex phases of the basis states. Under the choice presented in Table III, the most general contribution to the Hamiltonian takes the form

$$\mathcal{H}_D = \tau^x[\beta_x k_{y'}\sigma^x + \beta_y k_{x'}\sigma^y + \beta_z \delta k_z \sigma^z], \qquad (14)$$

where the coefficients $\beta_{x,y,z}$ are again to be determined from a comparison with the full model. The reduced Hamiltonian finally reads $\mathcal{H} = \mathcal{H}_0 + \mathcal{H}_S + \mathcal{H}_D$. It is a considerable simplification with respect to H, and it only contains nine parameters that need to be extracted from the full model.

C. Conditions for robust band touching

Band touching between the HOB and the LUB occurs in the full model when the two middle eigenvalues are equal in the simplified model. It can be shown that for a 4×4 matrix of the form $\mathcal{H}$ with $\beta_{x,y,z} \ll \alpha_{x,y}^{(1,2)}$, this is possible if and only if the direction of the vector $\vec{B} = (\beta_x k_{y'}, \beta_y k_{x'}, \beta_z \delta k_z)$

TABLE III. Potential terms in the Hamiltonian and their parities under the symmetry operations of the system: time reversal (T), reflection across the $\{y',z\}$ plane (R_1), reflection across the $\{x',z\}$ plane (R_2), and twofold rotation around the z axis (S).

	T	R_1	R_2	S
$k_{x'}$	−	−	+	−
$k_{y'}$	−	+	−	−
δk_z	−	+	+	+
σ^x	−	−	+	−
σ^y	−	+	−	−
σ^z	−	−	−	+
τ^x	+	−	−	+
τ^y	−	−	−	+
τ^z	+	+	+	+

lies halfway between the directions of the vectors $\vec{A}^{(1,2)} = (\alpha_x^{(1,2)}k_{x'}, \alpha_y^{(1,2)}k_{y'}, 0)$. The two bands then cross each other as $|\delta\vec{k}|$ is increased without changing the direction of $\delta\vec{k}$, whereas anticrossing happens otherwise. Since the above condition requires the three vectors to lie in the same plane, the third component of $\vec{B}$ has to vanish. Due to $\beta_z \neq 0$ in general, we find that robust band touching can only occur in the $\delta k_z = 0$ plane.

Restricting our attention to this plane simplifies the problem because $\vec{A}^{(1,2)}$ and $\vec{B}$ become 2D vectors. If we change the ratio $k_{y'}/k_{x'}$ gradually from 0 to ∞, the ratios of the corresponding components in $\vec{A}^{(1,2)}$ change in the same direction, while those in $\vec{B}$ change in the opposite direction between 0 and $\pm\infty$. This means that whether band touching happens at any $\delta\vec{k}$ is determined entirely by the signs of the different parameters. Since we always choose $\alpha_{x,y}^{(1,2)} > 0$, the condition becomes straightforward: band touching occurs if and only if β_x and β_y have the same sign.

Let us now consider the special case of the symmetric potential with $\delta_0 = 0$. By repeating the symmetry considerations in Sec. III B and taking into account the additional fourfold roto-reflection symmetry around the z axis, we find that the parameters from the full model are no longer independent because $\alpha_x^{(1,2)} = \alpha_y^{(1,2)}$ and $\beta_x = -\beta_y$. This shows that band touching can only occur in this scenario if at least one of these parameters vanishes. However, the corresponding band touching is not robust because it requires the fine tuning of a parameter. We conclude that robust band touching requires the asymmetry characterized by $\delta_0 \neq 0$, and expect that it becomes easier to observe as U_0 and δ_0 increase.

D. The Weyl semimetal phase

The detailed behavior of the system is determined by how the coefficients from the full model depend on the external parameters. Since this dependence is affected by the complexity of the full model, its understanding requires a numerical treatment. In perspective of this, we numerically investigate the phenomenon of robust band touching in the function of the layer thicknesses $N_{1,2}$, the strain $\epsilon_0 \equiv \epsilon(\mathrm{HgTe})$ in the multilayer structure, the amplitude U_0 of the superlattice potential, and the asymmetric displacement δ_0.
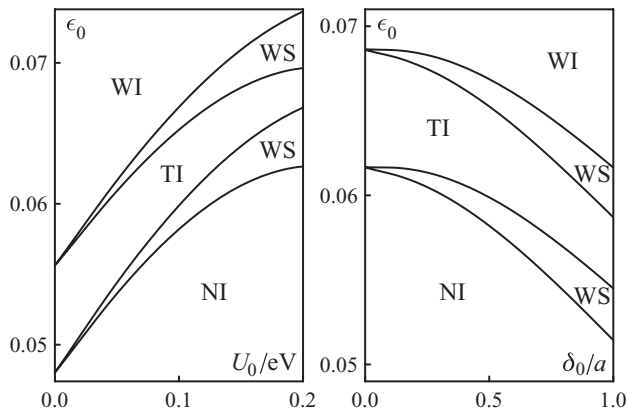
FIG. 2. Critical strains ϵ_0 against U_0 at constant $\delta_0 = a/2$ (left) and against δ_0 at constant $U_0 = 0.1$ eV (right). The phase boundaries separate four distinct phases: the normal insulator (NI), the strong (3D) topological insulator (TI), the weak (2D) topological insulator (WI), and the Weyl semimetal (WS). The layer thicknesses are constant $N_1 = 3$ and $N_2 = 4$ in both subfigures.

We first consider the dependence on the strain. If $U_0 \neq 0$ and $\delta_0 \neq 0$, there are two ranges in ϵ_0 close to zero with band touching in the $k_z = 0$ and the $k_z = \pi/d$ planes, respectively. The corresponding band touching is robust because it remains intact for an infinitesimal change in any of the external parameters ϵ_0, U_0, and δ_0. The upper and lower limits of the ranges are functions of U_0 and δ_0 as illustrated in Fig. 2, and we verify the expectation from Sec. III C that the ranges increase with both U_0 and δ_0. For the reasonable values of $U_0 \sim 0.1$ eV and $\delta_0 \sim a/2$, the ranges are $\Delta\epsilon_0 \sim 0.002$.

Now we turn our attention to the layer thicknesses. Keeping the HgTe thickness $N_1 = 3$ constant and varying the CdTe thickness N_2 between 4 and 8 reveals that an increase in N_2 decreases $\Delta\epsilon_0$. This is intuitive because δ_0 becomes smaller in comparison to d. Keeping the CdTe thickness $N_2 = 4$ constant and varying the HgTe thickness N_1 between 3 and 7 shows that an increase in N_1 shifts the ranges in ϵ_0 downwards. This means that the phases with robust band touching appear at more negative strains.

To conclude that these phases are indeed Weyl semimetals, they need to satisfy one more condition: the lack of band overlap. Even if there is robust band touching between the HOB and the LUB, the band structure becomes metallic if the highest overall energy of the HOB is larger than the lowest overall energy of the LUB. It is an empirical observation that the individual band structures of the $k_z = 0$ and the $k_z = \pi/d$ planes are metallic when ϵ_0 is sufficiently negative. This occurs for all $\epsilon_0 < 0$ in the limit of $U_0 \rightarrow 0$ or $\delta_0 \rightarrow 0$, while the critical ϵ_0 becomes slightly negative at larger values of U_0 and δ_0. Furthermore, the appropriate bands of the $k_z = 0$ and the $k_z = \pi/d$ planes can overlap with each other as well. Since the band-touching energies are different in the two planes, this typically occurs when there is band touching in one of the planes and almost band touching in the other one.

We are now in the position to discuss the other phases around the Weyl semimetals. The overall transition between the two bulk phases at small and large values of ϵ_0 is a 2D topological phase transition because it happens via band touching around both special points on the k_z axis. This means
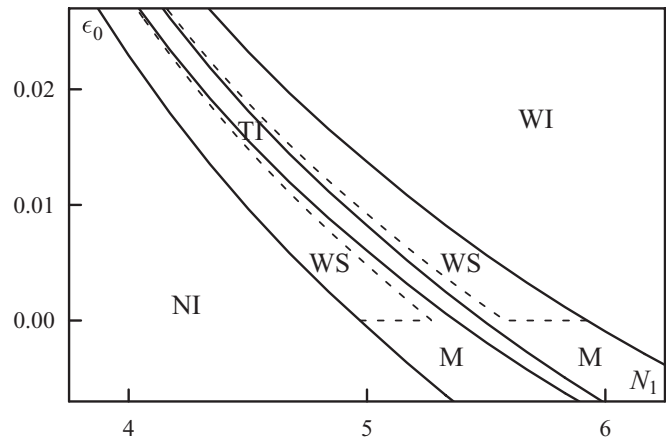

FIG. 3. Phase diagram of the system against the strain ϵ_0 and the HgTe thickness N_1. The other parameters are constant: $U_0 = 0.2$ eV, $\delta_0 = a/2$, and $N_2 = 4$. The phase boundaries separate five distinct phases: the normal insulator (NI), the strong (3D) topological insulator (TI), the weak (2D) topological insulator (WI), the band overlap metal (M), and the Weyl semimetal (WS). The dashed lines indicate approximate phase boundaries.

that the bulk phases on the two sides of this transition do not have a 3D topological character: we identify them as the NI phase and the weak (2D) topological insulator (WI) phase. Since the spin-orbit coupling is stronger in HgTe than in CdTe, we argue that the system is in the NI phase when the HgTe layers are thin and in the WI phase when the HgTe layers are thick.[4] On the other hand, the phase between the Weyl semimetals is related to each bulk phase by a topological phase transition that has a 3D character because it happens via band touching around only one special point. We conclude that this phase in the middle is the TI phase. Note that the NI and the WI phases are equivalent in terms of their 3D topology, therefore there is no need to distinguish between the two Weyl semimetals: they are intermediates in two equivalent phase transitions.

The phase diagram of the system against the strain ϵ_0 and the HgTe thickness N_1 is presented in Fig. 3. Since its boundaries are interpolated from only five points corresponding to integer values of N_1, the phase diagram is only correct on the qualitative level. Nevertheless, it provides useful guidelines for the realization of the Weyl semimetal phase in this multilayer structure. The strain ϵ_0 has to be positive to avoid band overlap but not too large because that would be hard to achieve experimentally. This gives a restriction on the thickness of the HgTe layers: the ideal dimensionless thickness of $4 \leqslant N_1 \leqslant 6$ corresponds to an actual thickness of $d_1 \sim 3$ nm, which is on the border of experimental reasonability.

E. Connection with the superlattice model

To illustrate the relationship with the results obtained in Sec. II, we discuss the arrangement of the Weyl points in the Weyl semimetal phase. There are four Weyl points that are related to each other by the symmetries of the system. As ϵ_0 is gradually increased, and the transition from the NI (TI) phase to the TI (WI) phase happens through a Weyl semimetal, the Weyl points first appear at the $k_{x'} = 0$ line,

move on approximately circular curves, and finally disappear at the $k_{y'} = 0$ line. This is in perfect agreement with the corresponding arrangement for the superlattice model in Sec. II D. Indeed, the two models presented in Secs. II D and III A obey the same symmetries, therefore it is understandable that their low-energy features are equivalent.

The comparison of the band structures in Secs. II A and III B also makes it possible to estimate reasonable values for the superlattice parameters in Eq. (1). The inversion-breaking voltage V corresponds to the energy difference $E^{(1)} - E^{(2)}$ between the HOB and the LUB, which is typically about 0.05 eV in the tight-binding model. The Fermi velocity of the surface states becomes $v_F \sim \alpha_{x,y}^{(1,2)} \sim 10^6$ ms^{-1}, and the hopping amplitudes are estimated from the typical energy scale along the k_z axis: $\Delta_{T,N} \sim 10^{-3}$ eV. The small magnitude of $\Delta_{T,N}$ indicates that the band structure is relatively flat in the k_z direction. Since $v_r = v_F \sim 10^6$ ms^{-1}, and $d \sim 10$ nm gives $v_z = d\sqrt{\Delta_T \Delta_N} \sim 10^4$ ms^{-1}, this results in the relation $v_z \ll v_r$ between the effective Fermi velocities around the Weyl points. Note that the energy scale $\Delta_{T,N}$ also translates into a maximal temperature $T \sim 10$ K at which the Weyl semimetal phase is experimentally observable in this multilayer structure.

IV. PHYSICAL CHARACTERISTICS

A. Conductivity anisotropy

It was shown in Ref. 8 that the Weyl semimetal phase is metallic: when impurities are present, its conductivity is a finite constant in the limit of zero temperature. Using the Boltzmann equation, one finds a conductivity $\sigma = e^2 v^2 / 6\pi\gamma$ for each Weyl point, where v is the effective Fermi velocity and γ is the strength of the impurity potential. This finite conductivity is a characteristic experimental feature, especially in contrast with the neighboring NI and TI phases. In this subsection, we demonstrate that the finite conductivity at $T \to 0$ becomes highly anisotropic when the Weyl semimetal phase occurs due to broken inversion symmetry.

To achieve this, we consider the model in Sec. II D, and derive an expression for the conductivity tensor in the limit of small $\delta_T - \delta_N$. When the condition of the Weyl semimetal phase is satisfied, there are four Weyl points at angles $\theta_1 = \theta$, $\theta_2 = -\theta$, $\theta_3 = \pi + \theta$, and $\theta_4 = \pi - \theta$. Due to the convention $0 \leqslant \theta \leqslant \pi/2$ we find that θ gradually decreases from $\pi/2$ to 0 during a transition from the NI phase to the TI phase. For each Weyl point labeled by l, the conductivity tensor in the (x,y,z) basis takes the form[8]

$$\sigma_l = \frac{e^2}{6\pi\gamma} \begin{pmatrix} v_r^2 \cos^2\theta_l & v_r^2 \cos\theta_l \sin\theta_l & 0 \\ v_r^2 \cos\theta_l \sin\theta_l & v_r^2 \sin^2\theta_l & 0 \\ 0 & 0 & v_z^2 \end{pmatrix}, \quad (15)$$

where we exploit $v_t \ll v_r$ relating the effective Fermi velocities. Adding the contributions of all four Weyl points, there is a cancellation in the off-diagonal terms, and we obtain

$$\sigma = \sum_{l=1}^{4} \sigma_l = \frac{2e^2}{3\pi\gamma} \begin{pmatrix} v_r^2 \cos^2\theta & 0 & 0 \\ 0 & v_r^2 \sin^2\theta & 0 \\ 0 & 0 & v_z^2 \end{pmatrix}. \quad (16)$$

As the transition between the NI and the TI phases takes place through the Weyl semimetal phase, the conductivities in the x and y directions change in a complementary fashion. In
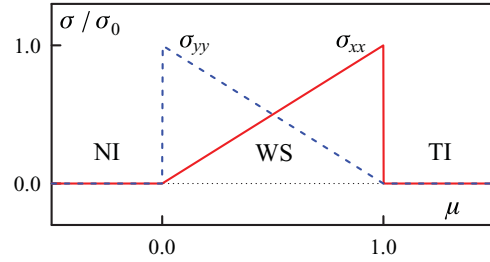

FIG. 4. (Color online) Variation in the principal conductivities σ_{xx} (red solid line) and σ_{yy} (blue dashed line) during a transition between the normal insulator (NI) and the topological insulator (TI) phases through the Weyl semimetal phase (WS). The transition parameter is $\mu = v_F^2(\Delta_N^{(0)} - \Delta_T^{(0)})/[V^2(\delta_T - \delta_N)]$ and the conductivities are measured in units of $\sigma_0 = 2e^2 v_F^2 / 3\pi\gamma$.

particular, σ_{xx} vanishes on the NI side and σ_{yy} vanishes on the TI side of the Weyl semimetal phase. For an illustration, see Fig. 4. The conductivity in the z direction is approximately constant with $\sigma_{zz} \ll \sigma_{xx}, \sigma_{yy}$ due to $v_z \ll v_r$. Such a strong conductivity anisotropy that depends sensitively on the system parameters is a potential hallmark of a Weyl semimetal with broken inversion symmetry.

B. Topological surface states

Since Weyl semimetals are topological phases of matter, they are characterized by topological surface states.[8] In this subsection, we consider the model in Sec. II D, and demonstrate the existence of these surface states. Although we choose a specific situation and also make a couple of simplifying assumptions in the following, the topological nature of the surface states ensures that they exist under more generic circumstances as well.

In our specific situation, the interface is in the $\{x,z\}$ plane, therefore any spatial variation is in the y direction only. This implies that k_x and k_z are still valid quantum numbers. Since $\Delta_{T,N}$ in Eq. (7) do not depend on k_y, we can determine the surface states without taking the explicit **k** dependence into account, and then simply substitute the appropriate values $\Delta_{T,N}$ for each k_x. It is assumed that only Δ_T changes with y and the other parameters are constant: $\Delta_T < \Delta_N$ at $y \to -\infty$, $\Delta_T = \Delta_N$ at $y = 0$, and $\Delta_T > \Delta_N$ at $y \to +\infty$. Furthermore, if Δ_T changes sufficiently slowly, we can approximate it with a linear function in the important region around $y = 0$: we write $\Delta_T - \Delta_N = Ky$. Expanding the k_z-dependent terms up to first order in $k_z' \equiv k_z - \pi/d$, we find that the surface states $|\Psi\rangle$ with energy E need to satisfy

$$E|\Psi\rangle = \left[v_F \tau^z (-i\sigma^x \partial_y - \sigma^y k_x) + V\tau^z \right. $$
$$\left. + Ky\,\tau^x + k_z' d\,\Delta_N\,\tau^y \right] |\Psi\rangle, \quad (17)$$

along with $|\Psi\rangle \to 0$ in the limits of $y \to \pm\infty$. To make the subsequent discussion of the surface states more transparent, we introduce the dimensionless form

$$\tilde{E}|\Psi\rangle = [\tau^z (-i\sigma^x \partial_{\tilde{y}} - \sigma^y \kappa_x) + \tilde{V}\tau^z + \tilde{y}\,\tau^x + \kappa_z \tau^y]|\Psi\rangle, \quad (18)$$

where the variables $\tilde{y} = y\sqrt{K/v_F}$, $\tilde{E} = E/\Lambda$, $\tilde{V} = V/\Lambda$, $\kappa_x = v_F k_x/\Lambda$, and $\kappa_z = k_z' d\,\Delta_N/\Lambda$ are all dimensionless, while $\Lambda = \sqrt{K v_F}$ is a characteristic energy scale.

As a starting point in our discussion, we consider the limit of $\tilde{V} = 0$. In this case, there are two distinct surface state solutions for each κ_x and κ_z that take the analytic form

$$|\Psi\rangle = (i, \mp i e^{i\varphi}, \mp e^{i\varphi}, 1)\exp\left(-\frac{\tilde{y}^2}{2}\right) \qquad (19)$$

in the (T↑, T↓, B↑, B↓) basis, where $\tan\varphi = \kappa_x/\kappa_z$ and the letters T/B stand for the top/bottom surfaces. The corresponding dimensionless energies $\tilde{E} = \pm\sqrt{\kappa_x^2 + \kappa_z^2}$ are indicative of surface states with Dirac dispersion between NI and TI phases of matter. In the more relevant case of $\tilde{V} \neq 0$, these analytic solutions only find straightforward generalizations for $\kappa_x = 0$ when

$$|\Psi\rangle = (i, \mp i, \mp 1, 1)\exp\left(-\frac{\tilde{y}^2}{2} \pm i\tilde{V}\tilde{y}\right) \qquad (20)$$

and the dimensionless energies are $\tilde{E} = \pm\kappa_z$. Note that these surface states decay in an oscillating fashion at $y \to \pm\infty$, and the wave vector $k_y = \pm V/v_F$ of the oscillations corresponds to the radius of the circle in the $k_z = \pi/d$ plane along which band touching occurs, as described in Sec. II.

In the most generic case of $\tilde{V} \neq 0$ and $\kappa_x \neq 0$, we solve Eq. (18) numerically and find that there are still two distinct surface states $|\Psi\rangle$ for each κ_x and κ_z. The ratios of the vector components in $|\Psi\rangle$ are no longer independent of $\tilde{y}$, which explains why simple analytic solutions like those in Eqs. (19) and (20) cannot be obtained. We verify that the surface states follow a Dirac dispersion at small momenta $\kappa_{x,z} \ll 1$, even when the dimensionless voltage $\tilde{V}$ is large. However, the effective Fermi velocity in the κ_x direction is reduced by a factor that is empirically found to be $\exp(-\tilde{V}^2)$, and hence the dispersion relation at small $\kappa_{x,z}$ becomes

$$\tilde{E} = \pm\sqrt{\kappa_x^2 \exp(-2\tilde{V}^2) + \kappa_z^2}. \qquad (21)$$

Unlike in the κ_z direction where the analytic solution guarantees the linearity of the dispersion for all κ_z, there is a deviation from the linear dispersion in the κ_x direction. As illustrated in Fig. 5, the Dirac dispersion in Eq. (21) is only valid for small enough κ_x.
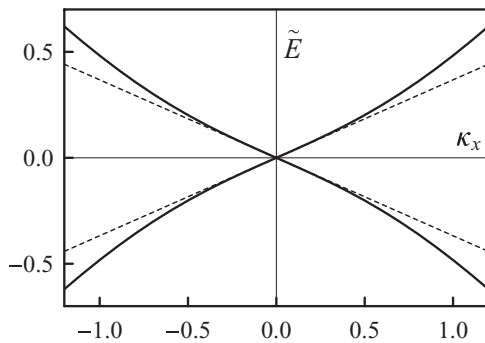

FIG. 5. Dimensionless energies of the surface states in the function of the momentum κ_x when $\kappa_z = 0$ and $\tilde{V} = 1$. The dashed lines are linear asymptotes given by Eq. (21) in the $\kappa_x \ll 1$ limit.

If we now restore the **k** dependence of $\Delta_{T,N}$, the surface states $|\Psi\rangle$ remain the same for each k_x. However, they only exist at those k_x for which the difference $\Delta_T - \Delta_N$ changes sign between $y \to \pm\infty$. Assuming without loss of generality that $\delta_T > \delta_N$ in Eq. (7) and that $\Delta_T^{(0)} - \Delta_N^{(0)}$ does change sign, we find that $\Delta_T > \Delta_N$ for all k_x at $y \to +\infty$, while $\Delta_T < \Delta_N$ is only true at $y \to -\infty$ for $|k_x| < k_0$. The critical momentum k_0 marks the equality $\Delta_T = \Delta_N$ at $y \to -\infty$, which is one of the conditions required for band touching in Sec. II. While the material at $y > 0$ is definitely in the NI phase, the material at $y < 0$ is in the Weyl semimetal phase if $k_0 < V/v_F$ so that band touching occurs, and it is in the TI phase if $k_0 > V/v_F$ so that band touching does not occur. In the former case, surface states exist between the coordinates $k_x = \pm k_0$ of the Weyl points. As the Weyl points first appear at the $k_x = 0$ line, and then start to move further away from it, the range in k_x increases and more surface states appear. Remarkably, this range characterized by k_0 further grows when the material at $y < 0$ is already in the TI phase, and there is no band touching at all.

V. SUMMARY

We proposed a time-reversal invariant realization of the Weyl semimetal phase that occurs due to broken inversion symmetry. We considered both a superlattice model adapted from Ref. 8 and a tight-binding model describing an experimentally reasonable HgTe/CdTe multilayer structure. The superlattice model was suitable for analytic calculations due to its simplicity, while the more realistic tight-binding model required a numerical treatment.

Although the formulations of the two models are very different, their identical symmetries lead to equivalent low-energy features. It should be remarked that, as seen from the generality of the superlattice model, the Weyl semimetal could be achieved in many possible material structures. Exploration of potential compounds other than HgTe/CdTe would be extremely interesting, especially given the need to tune strain in the latter to observe the desired physics.

For both models considered, we found a Weyl semimetal phase between the NI and the TI phases. This phase is characterized by a finite number of Weyl points with robust band touching at the Fermi level: the band touching occurs for a finite range of the system parameters, and hence it cannot be removed by an infinitesimal perturbation. We further verified that the band-touching points are proper Weyl points with a linear dispersion relation around them.

In terms of experimental observation, the potential hallmarks of the Weyl semimetal phase with broken inversion symmetry are a strong conductivity anisotropy and the presence of topological surface states. The highly unconventional low-temperature and low-frequency bulk transport is discussed in Ref. 14. The Dirac dispersion relation of the surface states is indicative of TI materials, but these surface states only exist in a region of momentum space that is determined by the positions of the Weyl points. The Weyl semimetal phase between the NI and the TI phases described in this paper is therefore qualitatively new in terms of its topological surface states as well.

[1]M. Z. Hasan and C. L. Kane, Rev. Mod. Phys. **82**, 3045 (2010).

[2]D. J. Thouless, M. Kohmoto, M. P. Nightingale, and M. den Nijs, Phys. Rev. Lett. **49**, 405 (1982).

[3]C. L. Kane and E. J. Mele, Phys. Rev. Lett. **95**, 226801 (2005); B. A. Bernevig and S.-C. Zhang, *ibid*. **96**, 106802 (2006).

[4]B. A. Bernevig, T. L. Hughes, and S.-C. Zhang, Science **314**, 1757 (2006).

[5]J. E. Moore and L. Balents, Phys. Rev. B **75**, 121306(R) (2007); L. Fu, C. L. Kane, and E. J. Mele, Phys. Rev. Lett. **98**, 106803 (2007); R. Roy, Phys. Rev. B **79**, 195322 (2009).

[6]M. König, S. Wiedmann, C. Brüne, A. Roth, H. Buhmann, L. W. Molenkamp, X.-L. Qi, and S.-C. Zhang, Science **318**, 766 (2007); D. Hsieh, D. Qian, L. Wray, Y. Xia, Y. S. Hor, R. J. Cava, and M. Z. Hasan, Nature (London) **452**, 970 (2008).

[7]X. Wan, A. M. Turner, A. Vishwanath, and S. Y. Savrasov, Phys. Rev. B **83**, 205101 (2011); K.-Y. Yang, Y.-M. Lu, and Y. Ran, *ibid*. **84**, 075129 (2011).

[8]A. A. Burkov and L. Balents, Phys. Rev. Lett. **107**, 127205 (2011).

[9]S. Murakami, New J. Phys. **9**, 356 (2007).

[10]C. Herring, Phys. Rev. **52**, 365 (1937).

[11]X. Dai, T. L. Hughes, X.-L. Qi, Z. Fang, and S.-C. Zhang, Phys. Rev. B **77**, 125319 (2008).

[12]A. Kobayashi, O. F. Sankey, and J. D. Dow, Phys. Rev. B **25**, 6367 (1982).

[13]J. N. Schulman and Y.-C. Chang, Phys. Rev. B **33**, 2594 (1986).

[14]A. A. Burkov, M. D. Hook, and L. Balents, Phys. Rev. B **84**, 235126 (2011).